Austenite reversion and nano-precipitation during a compact two-step heat treatment of medium-Mn steel containing Cu and Ni

Article *in* Journal of Materials Research and Technology · February 2022

DOI: 10.1016/j.jmrt.2022.02.008

5 authors, including:

Zigan Xu
RWTH Aachen University
6 PUBLICATIONS **25** CITATIONS
SEE PROFILE

Xiao Shen
RWTH Aachen University
5 PUBLICATIONS **19** CITATIONS
SEE PROFILE

Wenwen Song
RWTH Aachen University
51 PUBLICATIONS **540** CITATIONS
SEE PROFILE

Available online at www.sciencedirect.com

jmr&t Journal of Materials Research and Technology

journal homepage: www.elsevier.com/locate/jmrt

Original Article

Austenite reversion and nano-precipitation during a compact two-step heat treatment of medium-Mn steel containing Cu and Ni

Zigan Xu [a], *Xiao Shen* [a], *Tarek Allam* [a,b], *Wenwen Song* [a,*], *Wolfgang Bleck* [a]

[a] *Steel Institute, RWTH Aachen University, 52072, Aachen, Germany*

[b] *Department of Metallurgical and Materials Engineering, Suez University, 43528, Suez, Egypt*

ARTICLE INFO

Article history:
Received 26 November 2021
Accepted 2 February 2022
Available online 10 February 2022

Keywords:
Medium-Mn steel (MMnS)
Austenite reversion
Nano-precipitation
Synchrotron X-ray diffraction
Three-dimensional atom probe tomography

ABSTRACT

Breaking the strength-ductility paradox of very-low (≤0.05 wt.%)-C medium (3–12 wt.%)-Mn steels (MMnS) has been a hard-wired topic, since in these steels multi-step heat treatments are usually required to obtain austenite for improved ductility and precipitates for higher strength. In this study, a compact two-step heat treatment comprising short (2 min) annealing and tempering was developed to investigate the synergetic effect of austenite reversion and nano-precipitation on the tensile behavior of a very-low-C MMnS containing 1.5 wt.% Cu and 1.5 wt.% Ni. The annealing step promoted considerable amount of reverted austenite (33 vol.%), and the annealing was short to prevent Cu and Ni from partitioning into austenite, since they were supposed to maintain in the ferrite phase and then promote the nano-precipitation in the subsequent tempering stage. During the subsequent tempering step, the nano-precipitates with Cu concentration of 20–50 at.% in the precipitation core and enriched with Cu, Ni, Al and Mn were observed in the ferrite phase. The volume fraction of reverted austenite reached 38.5 vol.% after tempering, which led to the ultimate tensile strength of 1222 MPa and total elongation of 29% by the transformation induced plasticity during plastic deformation. The current study demonstrates the beneficial influence of the compact two-step heat treatment on the austenite reversion and nano-precipitation behavior of very-low-C MMnS with the addition of Cu and Ni, which subsequently enables an enhanced strain hardening behavior, thereby improving the mechanical property profile of the MMnS.

* Corresponding author.
E-mail address: Wenwen.Song@iehk.rwth-aachen.de (W. Song).

https://doi.org/10.1016/j.jmrt.2022.02.008

1. Introduction

As a promising candidate of the third generation advanced high strength steels (AHSS), medium-Mn steel (MMnS) exhibits an excellent combination of strength and ductility, which can be attributed to the transformation-induced plasticity (TRIP)/twinning-induced plasticity (TWIP) effects of metastable retained austenite (RA) within a matrix of ductile ferrite and/or tempered martensite [1]. The forged MMnS are widely applied in automotive parts and offshore infrastructures [2,3]. The industrial utilization of MMnS is related to the manufacturing feasibility with respect to the content of C and Mn [4]. The deformation-induced martensite enriched with C restricts the cold-formability and deteriorates the weldability of the MMnS plates. The micro-segregation of Mn and the formation of complex precipitates during continuous casting deteriorate the hot ductility and cause the billets to become susceptible to hot cracking [5]. C and Mn are both key elements in increasing the volume fraction and stability of RA [6], which accounts for the TRIP effect and is a crucial parameter that affects the strength of MMnS. Thus, a new challenge is to improve the strength of MMnS with a very-low-C content (less than 0.05 wt.%). A potential solution is to strengthen the very-low-C MMnS with nano-precipitates [7–9], which has been proven to be an effective strengthening strategy. Compared with conventional precipitates, nano-precipitates are typically coherent or semi-coherent with the surrounding matrix, thus retarding the crack propagation by reducing the elastic interaction between the precipitates and matrix. The enhancement in ductility is generally achieved along with enhanced strength [10].

Co-precipitation is a promising strategy to develop high number density (10^{22}–10^{24}/m^3) nano-precipitates in AHSS [11–13]. Compared with the precipitation of a single type of nano-particles, the co-existence of multiple types of nano-precipitates is more attractive. This is because a superior combination of different properties may be obtained as a result of the synergistic combination of multiple types of nano-particles with different compositions, microstructures, and mechanical properties [14]. Furthermore, the co-existence of two or more precipitates can avoid the undesired coarsening behavior of the precipitates. On the one hand, one precipitate becomes the nucleation site of the other and prevents the coarsening by increasing the number density. On the other hand, the interstitial elements of one precipitate segregate at the interface of its co-precipitate and deteriorate the coarsening rate. For example, compared with the single Cu-rich precipitates, the co-precipitation of Cu and NiAl decreased the mean diameter of the nano-precipitates by 45 times [13]. Seol et al. [11] designed highly organized nanoparticle arrays with the co-precipitation of a Mo–V rich shell and Ti–C rich core. The core–shell structured co-precipitates approximately doubled the strength of an Fe-based alloy from 500 to 1000 MPa. However, the co-exitance of irregular-shaped primary carbides and/or inclusion precipitates, e.g., TiN and Al_2O_3 [15], which deteriorates the materials mechanical properties, should be controlled during solidification.

Recently, the co-precipitation of Cu-rich precipitates and NiAl intermetallics has been proven to be a representative approach for nano-precipitation design. These nano-precipitates are typically on a sufficiently fine diameter of less than 5 nm, and coherent with the body-centered cubic (bcc) ferrite/martensite matrix [16]. Zhang et al. [17] performed aging at 500 °C for 10 h on a Fe-2.5Cu-2.1Al-1.5Mn (at.%) alloy. Numerous precipitates, mainly comprising Cu, Ni, Al, and Mn, were observed using three-dimensional atom probe tomography (3D-APT). Moreover, the co-precipitation structure was maintained even after a prolonged aging process of 2000 h under 500 °C. With that aging, the growth and coarsening of the Cu-rich core were retarded by the NiAl (Mn) phase shell. Jiao et al. [18] investigated the synergistic alloying effect of Al, Ni, and Mn on the characteristics of Cu-rich precipitates. On the one hand, the Ni and Al atoms could segregate at the precipitate/matrix interfaces and decrease the interfacial energy. On the other hand, the precipitation of B2–NiAl particles could serve as the nucleation site and increase the number density of Cu-rich precipitates. Furthermore, the addition of Mn was found to be beneficial in decreasing the critical energy for nucleation [19]. Mn is energetically favored to segregate nano-particles, significantly increasing the driving force and reducing the strain energy, thereby increasing the particle number density of Cu-rich precipitates by more than an order of magnitude [20].

As a promising method to achieve higher yield strength, the strengthening by fine precipitates with the addition of Cu has also been utilized in MMnS [20–22]. The alloying of Cu and Ni yields additional functional properties. The corrosion resistance is typically improved with the addition of anti-corrosion elements, such as Cr and N, to austenitic MMnS [23], and individual or combined additions of Cr, Cu, and Al to high-Mn steels [24] and structural steels [25,26]. The anti-bacterial functions are obtained for austenitic stainless steels by adding an oversaturated amount of Cu [27]. However, limited research has been conducted on the effect of the addition of Cu and Ni on the austenite reversion in MMnS. In particular, those heat treatment process were designed with the aim of facilitating nano-sized precipitates in MMnS, but rather with a focus on the potential contribution of Cu and Ni alloying in tailoring the austenite fraction and stability.

To better understand the effect of Cu and Ni alloying on the austenite reversion in MMnS, a reference alloy (Fe-0.05C–7Mn-1.5Al-1.5Si-0.5Mo) with a very-low-C content was selected, and deliberately alloyed with 1.5 wt.% Cu and 1.5 wt.% Ni. A novel heat treatment procedure, with a combined short annealing and tempering (SAT) process, was utilized to coordinate the sequential austenite reversion and nano-precipitation. The microstructure evolution was investigated qualitatively and quantitatively using electron backscattered diffraction (EBSD) and high-energy synchrotron X-ray (SY-XRD) diffraction techniques. 3D-APT was applied to characterize the local chemical composition of nano-precipitates and elemental partitioning behavior across the γ/α phase boundary. The synergistic TRIP effect and precipitation strengthening on tensile properties of the investigated alloy are further discussed, providing a guideline for the alloying and processing design of very-low-C MMnS with enhanced strength and plasticity.

2. Experimental methods

2.1. Materials

Two steels Fe-0.05C–7Mn-1.5Al-1.5Si-0.5Mo-xCu-xNi (wt.%) with different Cu and Ni contents ($x = 1.5$ for the Cu-alloyed material and $x = 0$ for the reference material) were investigated. Herein, they are referred to as "1.5Cu1.5Ni" and "0Cu0Ni" alloys, respectively. The C contents were very low in both alloys. Al and Si were alloyed to suppress undesired carbide formation. Mo was alloyed to restrain the segregation of Mn at grain boundaries. In the 1.5Cu1.5Ni alloy, Ni was deliberately alloyed with an equal amount of Cu to prevent hot-crack failure of the forged blocks during hot work. The detailed description of the investigated alloy was reported in [28,29].

The raw smelting elements were provided by Haines & Maassen Metallhandelsgesellschaft mbH. The cast ingots were produced in a laboratory vacuum induction furnace and cast as two 18 kg ingots with the cross-sectional area of 100 × 100 mm^2. Subsequently, they were homogenized at 1250 °C for 8 h, and then hot-forged at 900–1100 °C into billets with the cross-sectional area of 40 × 60 mm^2 at the Semi-Product Simulation Centre of RWTH Aachen University. Table 1 lists the chemical compositions, the austenite start (A_{C1}) and finish (A_{C3}) temperatures of the investigated as-forged 1.5Cu1.5Ni and 0Cu0Ni alloys. The chemical composition was examined using pulse discrimination analysis by optical emission spectrometry (PDA-OES, OBLF company). The A_{C1} and A_{C3} temperatures of the forged materials were determined using a dilatometer (DIL-805A, Bähr company) at a constant heating rate of 3 °C/min.

2.2. Processing design

A duplex microstructure consisting of ultra-fine-grained (UFG) ferrite(α) + austenite(γ) is the target microstructure after annealing, with the aim of achieving good combination of strength and ductility [28,29]. This duplex matrix was developed during intercritical annealing through the austenite reversion of martensite, forming the initial microstructure of the as-hot-forged billets. Hot forging was performed at 900–1100 °C, followed by air cooling. Two heat treatment conditions were investigated, namely "SAT" and "SA", as shown in Fig. 1. Thermocalc equilibrium calculation was performed using the Thermocalc 2019b software with the TCFE7 database. The calculated result indicates that the Cu-rich precipitates may precipitate below 640 °C. A temperature of 700 °C was selected (above A_{C1} of both alloys) for the short annealing step, and that of 500 °C (below A_{C1} of both alloys) was selected for the tempering step. The "SAT" specimens underwent a two-step annealing process with no intermediate quenching. They were annealed at 700 °C for 2 min in a salt bath, and then directly tempered at 500 °C for 3 h in another salt bath, followed by water quenching to room temperature (RT). The "SA" specimens were annealed at 700 °C for 2 min in the salt bath, and then directly water-quenched to RT. Conducting heat treatments in a salt bath ensures a rapid and uniform heating within a short time, and the heat-treated specimens can reach the targeted temperature precisely without overheating.

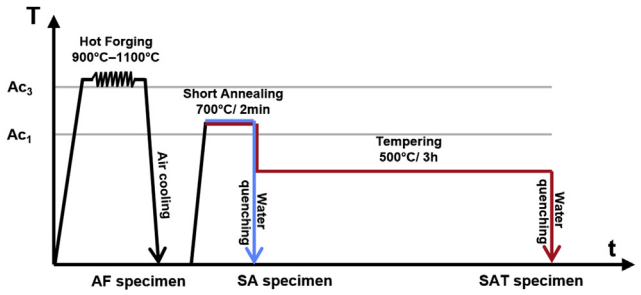

Fig. 1 – Schematic of materials processing. AF: as-forged; SA: short annealing; SAT: short annealing + tempering.

2.3. Materials characterization

The microstructures were characterized using EBSD analysis. The specimens were mechanically polished and electro-polished at 17 V for 15 s in the A2 solution, which was composed of 90 mL deionized water, 730 mL ethanol, 100 mL ethylene glycol monobutyl ether, and 78 mL perchloric acid. EBSD measurement was conducted using a ZEISS SIGMA field-emission scanning electron microscope (FE-SEM, Carl Zeiss Microscopy GmbH, Jena, Germany) at the Center for Digital Photonic Production (CDPP), RWTH Aachen University. The EBSD measurements were performed at electron energies of 20 keV, a working distance of 15 mm, and a step size of 50 nm. The EBSD result was acquired using Aztec V3.3 and analyzed using Channel 5 (Oxford instrument).

Compared with conventional XRD machines, high-energy SY-XRD enables the quantitative information of the constituent phases of larger volumes with higher statistical reliability [30]. The SY-XRD measurements were performed at beamline P02.1 (beam energy ~60 keV, wavelength 0.20740 Å, beam size 0.5 × 0.5 mm^2, penetrated specimen thickness 1.5 mm, dwell time 1 s) of PETRA III department, Deutsches Elektronen-Synchrotron Center (DESY) in Hamburg, Germany. The instrumental broadening and optics effects were calibrated using a LaB_6 standard specimen. The diffraction intensity was integrated along full azimuth angle with the Fit2D software [31]. The beam-stop sheltered area was excluded. The peaks corresponding to the austenite and ferrite phases within the 2θ angle range of 5–12° were identified according to

Table 1 – Chemical compositions (in wt.%) and transformation temperatures (in °C).

	C	Si	Mn	P	S	Ni	Mo	Cu	Al	N	A_{C1}	A_{C3}
1.5Cu1.5Ni	0.07	1.4	7.0	0.005	0.004	1.48	0.50	1.47	1.5	0.006	588	940
0Cu0Ni	0.05	1.5	7.0	0.005	0.004	0.01	0.51	0.01	1.5	0.006	600	1030

the standard crystallographic data obtained from the crystallography open database [32]. The MAUD software was used to index the constituent phases and calculate the phase fraction using the Rietveld refinement method [33].

3D-APT was employed to investigate the Cu precipitation, elemental partitioning, and segregation behavior in the austenite and ferrite duplex microstructure and grain boundary. The 3D-APT specimens were prepared by the lift-out and annular milling procedures using FEI® Helios™ Nanolab™ 660 focused ion beam. The 3D-APT measurements were conducted using a high-resolution local electrode atom probe (LEAP) 4000 XR instrument in the pulsed laser mode (laser pulse frequency 200 kHz, laser energy 30 pJ, base temperature 60 K, chamber pressure below 2×10^{-11} Pa). For the 3D reconstruction and analysis of the chemical composition, the visualization and analysis software from CAMECA named 'Integrated Visualization and Analysis Software' (IVAS® 3.80 software) was used in this study.

Tensile tests were conducted to evaluate the mechanical properties in a Z4204 tensile test machine at RT with a constant crosshead speed and an initial strain rate of 0.00025 s^{-1}. Bone-shaped plate tensile specimens were machined by wire cutting with a thickness of 1.5 mm and gauge length (L_0) of 13 mm. A video extensometer was utilized to measure the optical strain. After the tensile tests, another one set of repeated tests was performed to validate the reproducibility.

3. Results

3.1. Microstructure characterization

The austenite–ferrite phase transformation during the "SAT (short annealing and tempering)" and "SA (short annealing)" heat treatment processes was experimentally simulated in the dilatometer machine for the 1.5Cu15Ni-alloy, as illustrated in Fig. 2. The heating rate was set to 50 °C/s and the cooling rate was set to 150 °C/s to simulate the salt bath heating and water quenching treatments. A reference test of intercritical annealing was conducted at 700 °C for 3 h to check whether the austenite reversion reached equilibrium. As indicated by "arrow i" in Fig. 2a, the decrease in the sample length at 700 °C represents the $\alpha \rightarrow \gamma$ transformation. A more significant volume fraction of RA was obtained when annealing at 700 °C for 3 h, which could be deduced through the more considerable expansion decline of 39 μm compared to that of 11 μm in the sample annealed at 700 °C for 2 min. Consequently, the austenite reversion in the specimen annealed at 700 °C for 2 min did not reach equilibrium. In addition, as indicated by "arrow ii," the sample annealed at 700 °C for 2 min and tempered at 500 °C for 3 h demonstrated a small change in length when tempered at 500 °C, indicating the occurrence of phase transformation at 500 °C, which likely resulted from further austenite reversion or potential precipitation. Furthermore, as indicated by "arrow iii," no martensite transformation point was observed during the subsequent cooling process in the sample annealed at 700 °C for 2 min and tempered at 500 °C for 3 h and the sample annealed at 700 °C for 2 min. However, a noticeable M_s temperature was observed in the sample annealed at 700 °C for 3 h. Consequently, the RA in the sample annealed at 700 °C for 2 min and tempered at 500 °C for 3 h and that annealed at 700 °C for 2 min was fully retained at RT, since there is no sign for martensitic transformation based on the length change in the DIL curve during its cooling process. The change in length at the beginning (120 s–4000 s) of the tempering at 500 °C shown in Fig. 2b indicated that the austenite reversion at 700 °C was not complete, and continued during the tempering at 500 °C.

Except for the phase transformation simulation in the dilatometer machine, all the specimens were heat-treated in the salt-bath furnaces for microstructure and mechanical property characterization. Figure 3a depicts the SY-XRD spectra profile and Fig. 3b depicts the austenite fraction of the developed microstructure. For the 1.5Cu1.5Ni-alloy, the as-forged (AF) condition results in 3.6 vol.% austenite. After annealing at 700 °C for 2 min, 31.8 vol.% austenite was detected in the 1.5Cu1.5Ni-SA specimen. After tempering at 500 °C for 3 h, 38.5 vol.% austenite was detected in the 1.5Cu1.5Ni-SAT specimen, which was higher than the austenite fraction detected in the 1.5Cu1.5Ni-SA specimen. The increase in the austenite fraction indicated that the austenite reversion further proceeded during the tempering

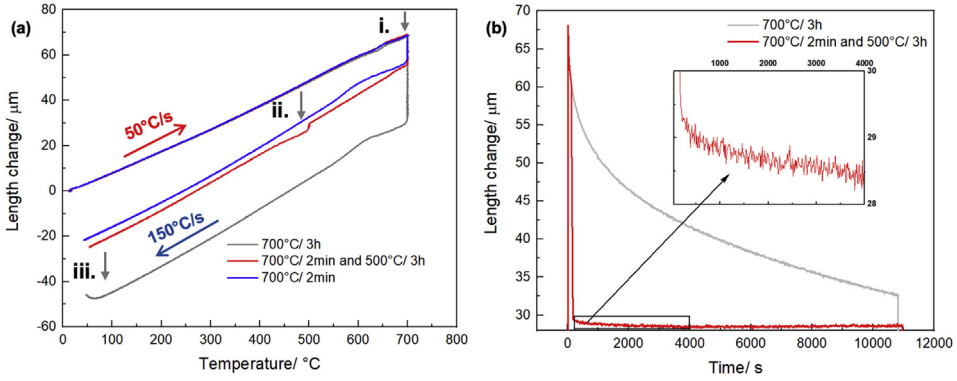

Fig. 2 – Dilatometry curves of the 1.5Cu1.5Ni-alloy: (a) Change in length with temperature; the arrows reflect the discussion in the text; arrow i: length changes of all three specimens at 700 °C, arrow ii: length change of the red curve at 500 °C, arrow c: length change of the grey curve at approximately 100 °C; (b) change in length with time; the inset highlights the transition during the tempering at 500 °C.

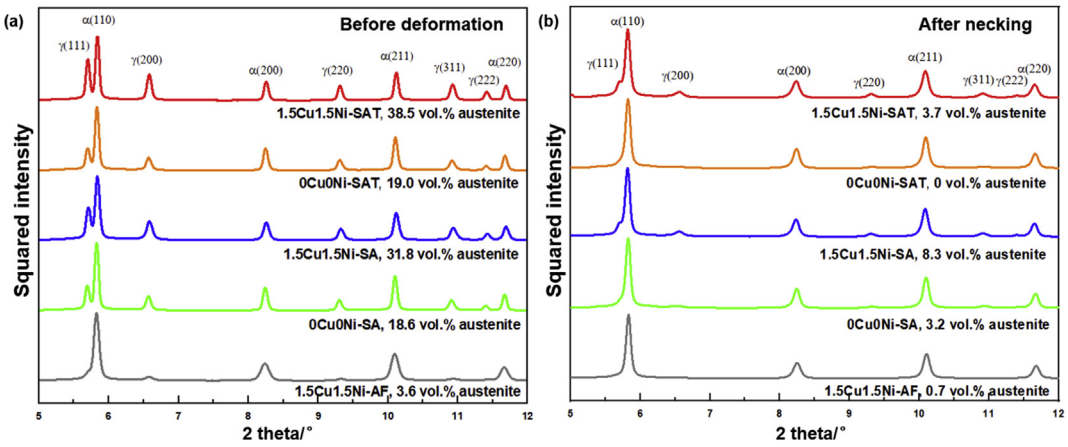

Fig. 3 – SY-XRD spectra of the microstructures: (a) before and (b) after tensile deformation.

step. For the 0Cu0Ni-alloy, 19.0 vol.% austenite was detected in the 0Cu0Ni-SAT specimen, which was slightly higher than the austenite fraction detected in the 0Cu0Ni-SA specimen (18.6 vol.%). The austenite reversion of the 1.5Cu1.5Ni-alloy during the tempering step was more effective than that of the 0Cu0Ni-alloy. Furthermore, the austenite fraction in the 1.5Cu1.5Ni-SAT specimen was twice as much as that in the 0Cu0Ni-SAT specimen. Compared with that of the 0Cu0Ni-alloy, the significantly increased austenite fraction in the 1.5Cu1.5Ni-alloy is attributed to Cu and Ni, which is discussed in detail in Section 4.1. The strong evidence of elemental partitioning in the microstructure constituents is described in detail based on the 3D-APT results in Section 3.2.

The morphologies of the developed microstructures in the 1.5Cu1.5Ni-alloy are illustrated in Fig. 4. The phase maps of the 1.5Cu1.5Ni-AF (Fig. 4a), 1.5Cu1.5Ni-SA (Fig. 4b), and 1.5Cu1.5Ni-SAT (Fig. 4c) specimens are superimposed with their image quality (IQ) maps. The phases indicated in green and red correspond to ferrite (BCC) and austenite (FCC), respectively. The 1.5Cu1.5Ni-AF specimen exhibited a fully martensite microstructure. Both the 1.5Cu1.5Ni-SA and 1.5Cu1.5Ni-SAT specimens revealed the presence of a UFG duplex microstructure comprising ferrite and austenite. The film-like austenite grains in the SA specimen were located along the martensite laths. After tempering for 3 h, the austenite fraction was significantly increased in the SAT specimen. The thickness of the austenite laths increased, and the austenite laths grew across the martensite laths to merge with the neighboring austenite films.

The characteristics of the austenite grains in the 1.5Cu1.5Ni-SAT and 1.5Cu1.5Ni-SA specimens are summarized in Table 2. The evaluation of listed information is obtained from software Channel 5 for EBSD analysis. The aspect ratio is defined using the ratio of the major to minor axis of the elliptical fit. ECD (equivalent circular diameter) refers to the diameter of a circle with an area equal to the area of the grain. The grain breadth is the shortest linear dimension of the grain calculated from the minimum diameter. The grain length is longest linear dimension of the grain calculated from the maximum diameter. The austenite laths in both specimens exhibited similar average aspect ratios. Compared with those of the 1.5Cu1.5Ni-SA specimen, the 1.5Cu1.5Ni-SAT specimen exhibited austenite grains with a larger average grain area and average equivalent circular diameter (ECD). The average lath breadth and length of the austenite laths in the 1.5Cu-SAT specimen were increased compared with those of the 1.5Cu-SA specimen. This indicates that during the direct tempering step, the RA laths grew not only along the direction of the ferrite laths, but also perpendicular to the lath boundaries.

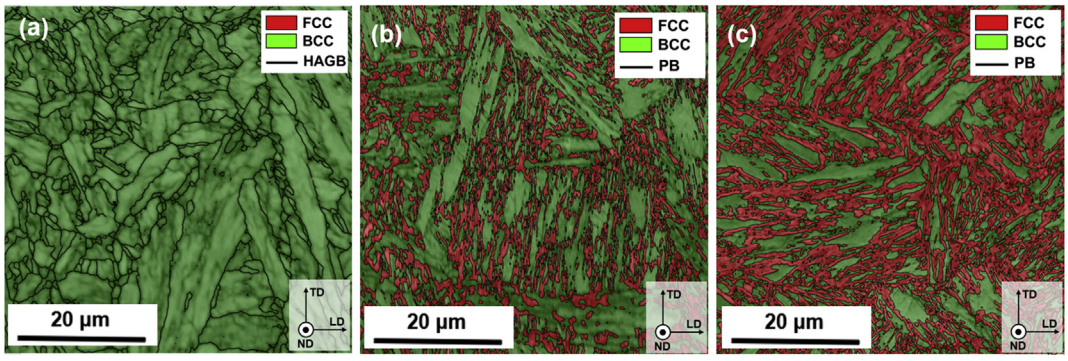

Fig. 4 – EBSD phase maps of (a) 1.5Cu1.5Ni-AF specimen; (b) 1.5Cu1.5Ni-SA specimen; (b) 1.5Cu1.5Ni-SAT specimen. FCC and BCC: the phase maps of FCC and BCC grains overlapped with their relating band contrast maps; HAGB: high angle grain boundary; PB: phase boundary.

Table 2 – Statistical information of austenite grains in 1.5Cu1.5Ni-SAT and 1.5Cu1.5Ni-SA specimens.

	Evaluated area	Number of grains	Average aspect ratio	Average grain area/μm^2	Average ECD/μm	Average lath breadth/μm	Average lath length/μm
1.5Cu1.5Ni-SAT	50 μm × 50 μm	563	2.62	4.16	1.65	1.60	3.58
1.5Cu1.5Ni-SA	50 μm × 50 μm	497	2.70	0.91	0.86	0.72	1.82

3.2. *Elemental partitioning*

Figure 5 depicts the reconstructed 3D-APT tips and concentration profile across the phase boundary. In the investigated specimens with a total Mn content of approximately 7 at.%, Mn partitions from the ferrite phase to the austenite phase at the nanometer scale. Iso-concentration surfaces of 4 at.% and 9 at.% Mn were applied for the visualization of ferrite (α) and austenite (γ) grains. For the 1.5Cu1.5Ni-SA specimen, the difference in Cu concentrations between austenite and ferrite was indefinable. However, for the 1.5Cu-SAT specimen, there was a noticeable difference in the Cu concentrations between austenite and ferrite. During tempering, the formation of Cu-rich precipitates consumed the Cu atoms in the ferrite matrix, resulting in an extremely low (< 0.2 at.%) Cu concentration, as shown by the orange curve in Fig. 5d. A strong phase boundary segregation of Mn was observed in the 1.5Cu1.5Ni-SAT specimen, but not in the 1.5Cu1.5Ni-SA specimen. During the tempering at 500 °C, the diffusivity of Mn was limited, causing the Mn atoms to enrich near the phase boundary. The enrichment of Mn near the grain boundary lowered the local A_{c1} temperature and proceed the austenite reversion [28], so that the austenite fraction increased from 33 vol.% to 38.5 vol.% during tempering. The C partition in the 1.5Cu1.5Ni-SAT specimen is more significant than that in the 1.5Cu1.5Ni-SA specimen, which improved the stability of the reverted austenite.

Table 3 summarizes the elemental concentration of austenite in 1.5Cu1.5Ni-SAT and 1.5Cu1.5Ni-SA specimens. To obtain statistical information, three regions-of-interest (ROIs) were investigated in each specimen. All the austenite stabilizing elements (C, Mn, Cu, and Ni) in the austenite phase were lower in the 1.5Cu1.5Ni-SAT specimen than in the 1.5Cu1.5Ni-SA specimen, which can be attributed to the significantly increased austenite fraction in the 1.5Cu1.5Ni-SAT specimen during its tempering step.

3.3. *Nano-precipitation characteristics*

The 3D-APT tips of 1.5Cu1.5Ni-SA and 1.5Cu1.5Ni-SAT specimens were acquired adjacent to the γ/α phase boundary to determine the atomic-scale compositional evolution during SAT treatment. The 3D atom maps of 1.5Cu1.5Ni-SA and 1.5Cu1.5Ni-SAT specimens are shown in

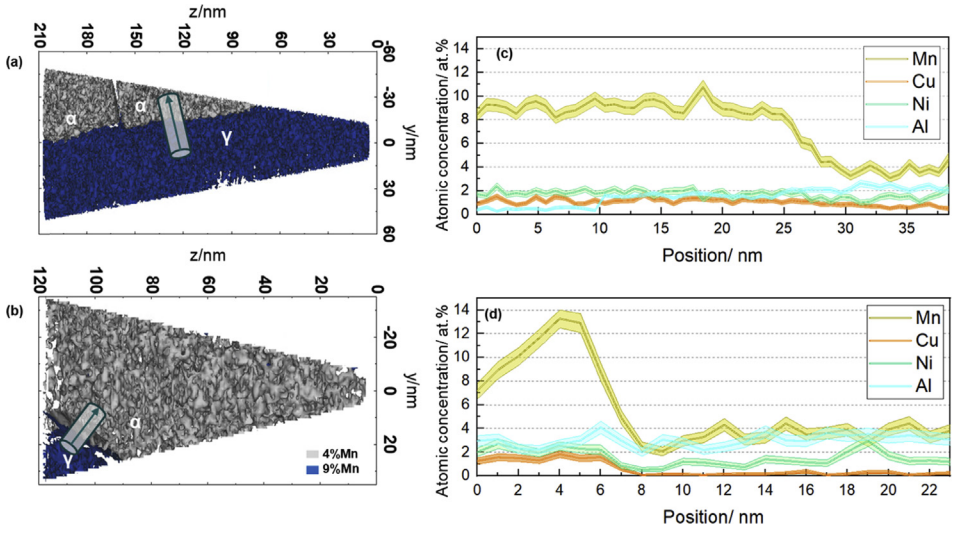

Fig. 5 – Elemental distribution of Mn and concentration profiles across phase boundary for (a, c) 1.5Cu1.5Ni-SA and (b, d) 1.5Cu1.5Ni-SAT specimens.

Table 3 – Elemental concentration of austenite in 1.5Cu1.5Ni-SAT and 1.5Cu1.5Ni-SA specimens.

		Mn	Cu	Ni	Al	C
1.5Cu1.5Ni-SAT	at.%	9.03 ± 0.31	1.43 ± 0.04	2.15 ± 0.12	2.84 ± 0.75	0.52 ± 0.05
	wt.%	9.19 ± 0.31	1.65 ± 0.04	2.23 ± 0.13	1.42 ± 0.37	0.11 ± 0.01
1.5Cu1.5Ni-SA	at.%	9.18 ± 0.28	1.47 ± 0.06	2.34 ± 0.07	1.61 ± 0.15	0.59 ± 0.05
	wt.%	9.30 ± 0.29	1.69 ± 0.06	2.40 ± 0.08	0.80 ± 0.08	0.13 ± 0.01

Fig. 6a and b, respectively. For the SA specimen, as shown in Fig. 6a, C, Mn, Cu, Ni, and Mo were enriched in the austenite grain (upper right), and Al was enriched in the ferrite grains. A slight grain boundary segregation of C, Mn, and Mo was observed between the two ferrite grains. No evident segregation was observed between the austenite and ferrite grains on the phase boundary. For the SAT specimen, besides the elemental partitioning of the above-mentioned elements, the segregation of C, Mn, and Mo was observed adjacent to the phase boundary due to the limited diffusivity. Moreover, the spherical nano-precipitates enriched with Cu, Ni, Al, and Mn could be obtained from the ferrite matrix, as shown in Fig. 6b.

The characteristics of the above-mentioned nano-precipitation of Cu, Ni, Al, and Mn atoms are presented in Fig. 7. The 12 at.% (Cu, Ni, and Al) iso-concentration surface was considered to represent the distribution of those precipitates, as shown in Fig. 7a. The 12 at.% Mn iso-concentration surface was employed as an indicator of γ/α phase boundary. Ninety-seven closed 12 at.% (Cu, Ni, Al) iso-concentration surfaces were identified in the ferrite matrix with a total volume of ~8.4×10^{-22} m^3. The number density of those Cu-rich precipitates was calculated as 1.15×10^{23} m^{-3}. Apart from the high number density of Cu-rich precipitates inside the ferrite matrix, an absence of the precipitates near the border of the ferrite matrix was noted, which could be due to the depleted Cu/Ni concentration. Both Cu and Ni tend to partition from ferrite to austenite, such that the ferrite border was short of Cu and Ni. Moreover, two precipitates were located on the phase boundary, which could be due to the elemental segregation on the phase boundary. Figure 7b shows the size distribution of the Cu-rich precipitates. The precipitate diameter was defined as that of the 12 at.% (Cu, Al, Ni) iso-concentration surface. The average diameter of the precipitates was 4.5 nm.

Three representative nano-sized co-precipitates in the 1.5Cu1.5Ni-SAT specimen are shown in Fig. 7c–e. In particular, two precipitates in the ferrite matrix with different sizes (P1 and P2, Fig. 7c and d) and one precipitate at the α/γ phase boundary (P3, Fig. 7e). Figure 7c shows a co-precipitation site with a diameter of approximately 4.5 nm enriched with Cu, Al, Ni, and Mn. The proxigram shows that Mn is slightly enriched (10 at.%) within the precipitate. Cu is highly enriched (50 at.%) in the center of the precipitate, while Ni and Al are enriched adjacent to the border of the precipitate. The concentration profile of ROI-1 shows that Ni and Al are enriched on one side of the precipitate (distance = 6 nm), while Cu is enriched on the other side of the precipitate (distance = 7.5 nm). For a small precipitate P2, with diameter approximately 2 nm in Fig. 7d, Al was the second major element (approximately 20 at.%) in the center of the precipitate; the first being Fe (approximately 50 at.%). Other precipitates in the ferrite matrix with the same diameter as P1 or P2 exhibited similar compositional characteristics. For precipitates as small as P2, Fe was the predominant element in the core of the precipitate, indicating that small precipitates are clusters of enriched Cu, Ni, Mn, and Al atoms. For large precipitates (e.g., P1), Cu was dominant in the center, and the atomic concentration of Fe sharply dropped to approximately 10 at.%. In contrast to Cu, Ni and Al were at the border of the precipitate, because Ni and Al could reduce the interfacial energy between the ferrite matrix and Cu-rich precipitates [20]. For the precipitate on the phase boundary P3, with diameter approximately 4 nm in Fig. 7e, although the size was as big as P1, the dominant element was still Fe (30 at.%).

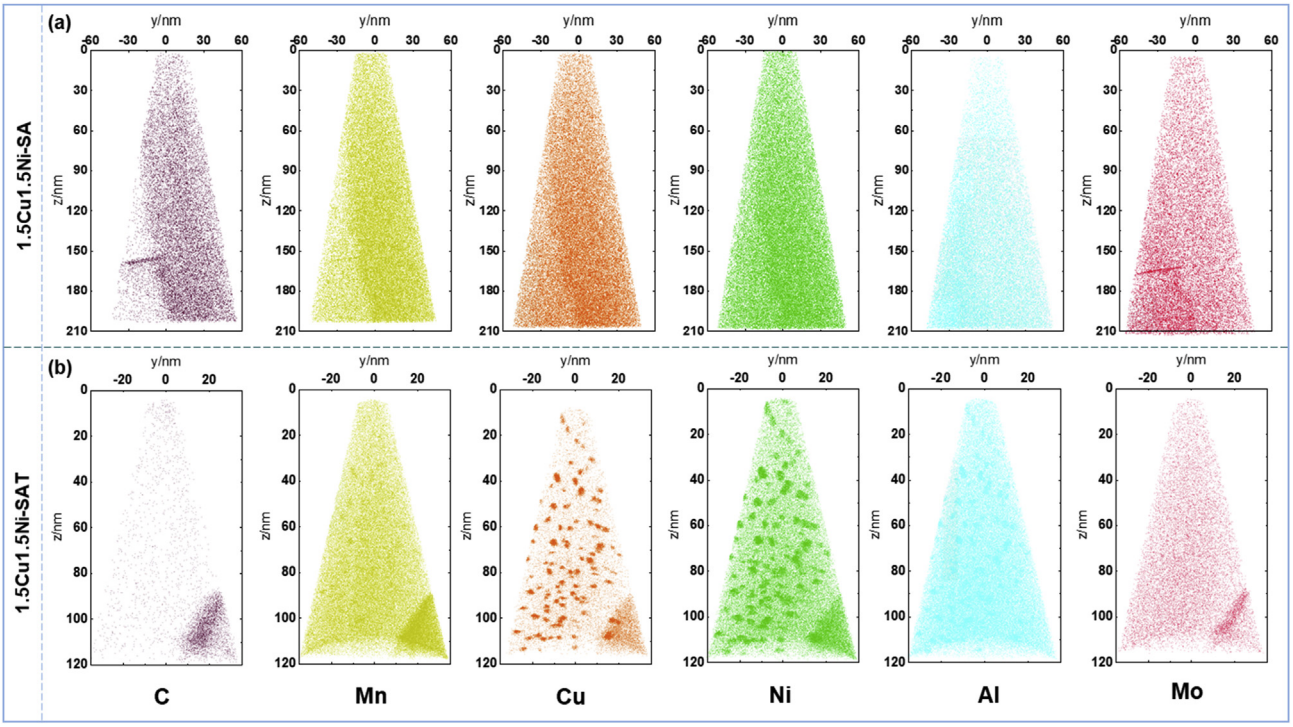

Fig. 6 – Atom maps of (a) 1.5Cu1.5Ni-SA and (b)1.5Cu1.5Ni-SAT specimens.

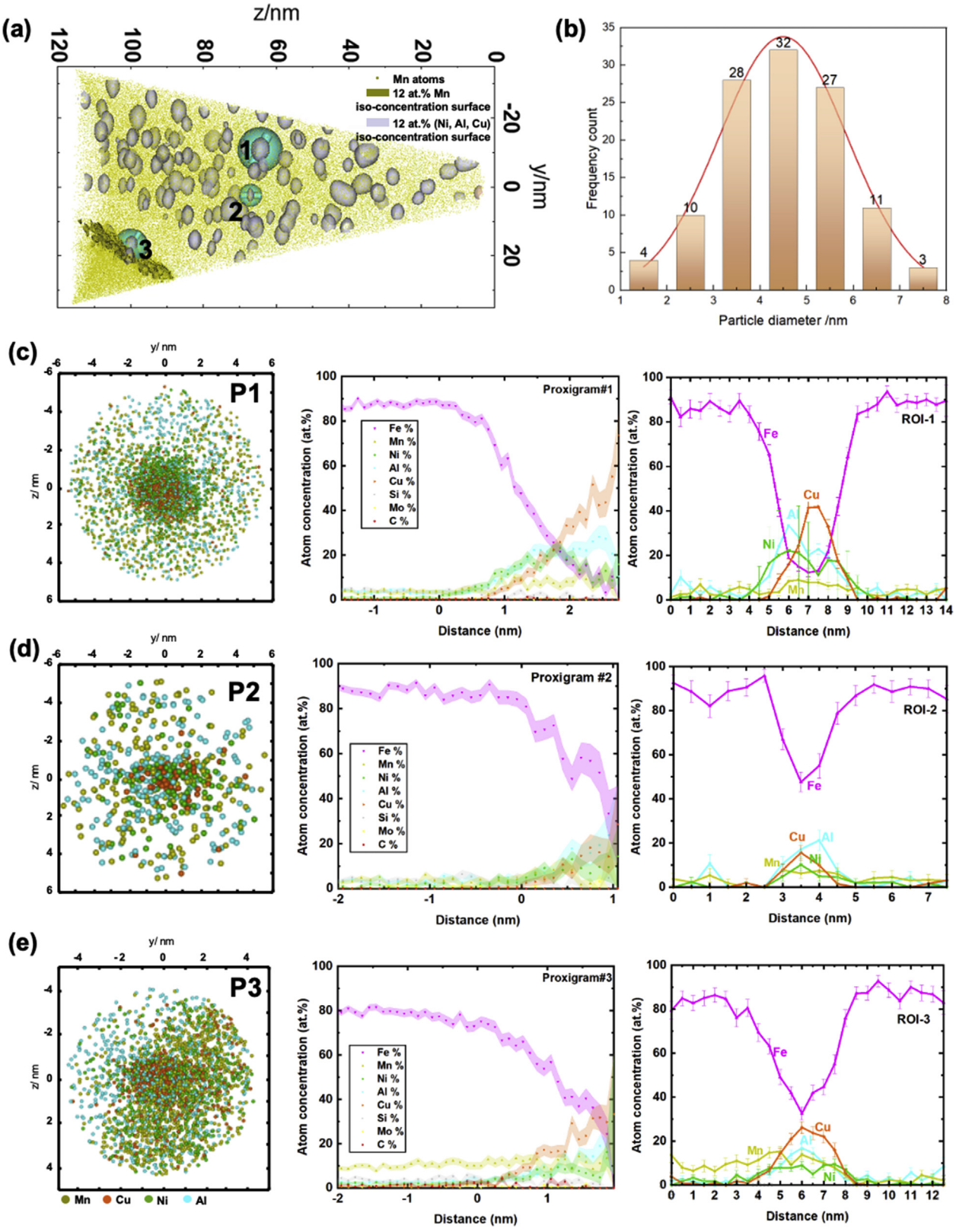

Fig. 7 – Local enrichment of Cu, Ni, Al, and Mn atoms in 1.5Cu1.5Ni-SAT specimen: (a) 12 at.% (Ni, Al, and Cu) iso-concentration surfaces and the location of three representative ROIs; (b) Size distribution of 12 at.% (Ni, Al, and Cu) iso-concentration surfaces; (c) Spatial element distribution of a 4 nm diameter particle in ferrite; (d) Spatial element distribution of a 2 nm diameter particle in ferrite; and (e) Spatial element distribution of a 5 nm diameter particle on γ-α phase boundary.

The precipitation of Cu-rich precipitates is a diffusion-controlled process where Cu atoms are decomposed as clusters and form bcc structured nano-precipitates from the supersaturated solid solution state [19]. These body-centered cubic (bcc) structured Cu-rich precipitates are coherent with the ferrite matrix [22], as also indicated from our synchrotron X-ray results. When more Cu atoms diffuse into these precipitates, Fe atoms are interstitially partitioned to the matrix, and such Cu-rich precipitates grow [16]. As a result, the cores of larger precipitates are enriched more with Cu atoms. The boundaries of these precipitates are enriched with Ni, Al, and Mn, since they act as a buffer layer to reduce the interfacial free energy between the bcc precipitates and the matrix [13]. Moreover, Ni and Al in the ferrite matrix can decrease the size of Cu-precipitates by increasing their number density [13].

In 1973, Goodman et al. [34,35] proved using APFIM that the earliest Cu precipitates are not of a single chemical composition of Cu, but Fe-rich Cu clusters. In 1990, Buswell et al. [36] used a TEM dark-field technique with the two-beam condition to demonstrate the precipitation of bcc Cu in bcc ferrite matrix. In 2007, Lee et al. [37] observed striations perpendicular to $[0\ 0\ 1]_\alpha$ in a dark-field image using $(2\ 0\ 0)_\alpha$ spot pointed out at the early stage of ageing at 500 °C, coherent bcc Cu clusters were formed. On prolonged ageing for 10 h, the twinned 9R Cu showing the characteristic herring-bone fringe formed. There is broad consent that, at the initial stages, Cu precipitates inherit the bcc structure of the α-Fe matrix, then it experiences partially or the full sequence of bcc–9R–3R (distorted face-centered cubic (fcc))–fcc structural change during transformation. Heo et al. [38] successfully revealed the sequence of the structural change during nano-sized Cu precipitation in 2013 and the formation of bcc Cu clusters was confirmed by direct HAADF-STEM imaging. Atom probe analysis (APFIM) reported that the early bcc Cu precipitates contain a significant portion of Fe, partly in excess of 50 at.% [34,39–43]. Using a Cahn-Hilliard-type analysis, Nagano and Enomoto [44] predicted that the Cu nucleus contains significant amounts of Fe in the very early stages. In the present work, considering the chemistry, size and morphology of the observed Cu particles (average diameter about 4.5 nm; spherical; 20–50 at.% Cu in the core and enriched with Ni, Mn and Al), they are most likely to be bcc at the early stage of Cu precipitation in the steels.

3.4. Tensile properties

Figure 8a shows the engineering tensile test curves of the investigated 1.5Cu1.5Ni- and 0Cu0Ni-alloys after the SA and SAT treatments, as well as the curves for the initial AF state. The tensile properties are summarized in Table 4.

For the 1.5Cu1.5Ni-alloy, the 1.5Cu1.5Ni-AF specimen exhibited a high yield strength of 987 MPa and a high ultimate tensile strength of 1257 MPa. However, the ductility was limited with a uniform elongation of 4.1% and total elongation of 12.7%. After the SA treatment, the 1.5Cu1.5Ni-SA specimen exhibited a drastically lower yield strength of 577 MPa and slightly lower ultimate tensile strength of 1107 MPa. The ductility of the SA specimen was improved with a uniform elongation of 15.5% and total elongation of 24.9%. After the SAT treatment, the 1.5Cu1.5Ni-SAT specimen exhibited a significantly higher yield strength of 848 MPa and ultimate tensile strength of 1222 MPa. Moreover, the ductility of the 1.5Cu1.5Ni-SAT specimen was improved with a uniform elongation of 20.1% and total elongation of 29.1%. In contrast to the 1.5Cu1.5Ni-SA specimen, the 1.5Cu1.5Ni-SAT specimen exhibited an extraordinary combination of significantly increased strength and improved ductility. Compared with the yield strength of the 1.5Cu1.5Ni-SA specimen, that of the 1.5Cu1.5Ni-SAT specimen was higher by 271 MPa, which is attributed to the precipitation-strengthening of nano-precipitates with high number density shown in Fig. 7.

For the 0Cu0Ni-alloy, the 0Cu0Ni-SAT specimen exhibited a yield strength of 692 MPa and ultimate tensile strength of 996 MPa, which was very close to those of the 0Cu0Ni-SA specimen. The tempering step was more crucial for improving

Table 4 – Tensile properties. ($R_{p0.2}$: yield strength, R_m: ultimate tensile strength, A_g: uniform elongation, A_{20}: total elongation).

Specimen	$R_{p0.2}$/MPa	R_m/MPa	A_g/%	A_{20}/%
1.5Cu1.5Ni-AF	987	1257	4	13
0Cu0Ni-AF	849	1123	4	12
1.5Cu1.5Ni-SAT	848	1222	21	29
1.5Cu1.5Ni-SA	577	1107	16	25
0Cu0Ni-SAT	692	996	18	28
0Cu0Ni-SA	644	964	15	23

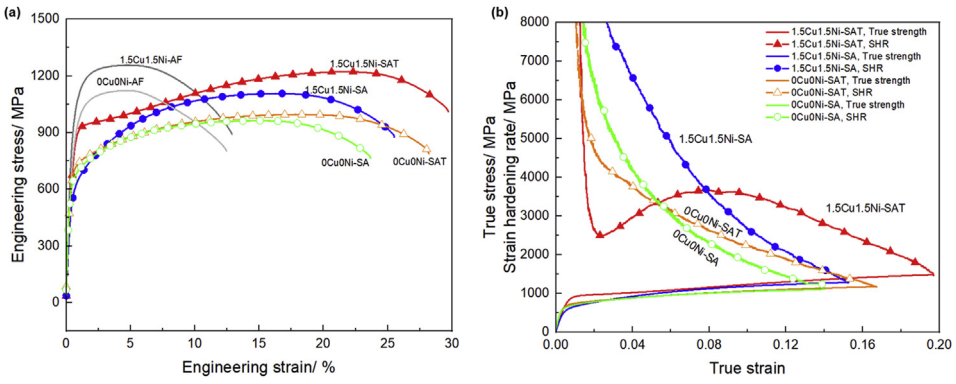

Fig. 8 – Tensile properties of investigated materials: (a) Engineering stress–strain curves; (b) True stress–strain and strain hardening curves.

the yield strength of the 1.5Cu1.5Ni-alloy than the 0Cu0Ni-alloy.

Figure 8b shows the true stress–strain curves superimposed with the strain hardening curves. Considering the austenite fraction before deformation and after necking in Fig. 3, the strain-hardening of all the four specimens in Fig. 8b are benefited from the significant TRIP effect. During plastic deformation, the 1.5Cu1.5Ni-SAT specimen exhibited unique strain hardening curve in Fig. 8b. As the applied strain increased, the strain hardening rate of the 1.5Cu1.5Ni-SAT specimen first decreased to 2500 MPa when the true strain reached 0.02, and then gradually increased to its maximum of approximately 3500 MPa at the true strain of 0.08, before finally gradually decreasing to 1450 MPa at the true strain of 0.19. Under all the other three conditions (1.5Cu1.5Ni-SA, 0Cu0Ni-SAT, and 0Cu0Ni-SA), their strain hardening rate oscillated until they reached their maximum true strain. Besides the TRIP effect, the outstanding strain hardening behavior of the 1.5Cu1.5Ni-SAT specimen also benefited from the interaction of dislocations and its nano-precipitates. When the dislocation encountered a Cu-rich precipitate, the precipitate became the obstacle for the dislocation movement. With the increase of plastic strain, the dislocation cut through the precipitate [45] and sheared their lattice structure [46]. The resistance of these bcc Cu precipitates to the moving dislocations is size-dependent. With the increase of the diameter, the bcc precipitates enriched with more Cu atoms, and became easier to be sheared [16]. Considering the size distribution of these bcc Cu-rich precipitates in Fig. 7b, the moving dislocations cut through these precipitates at different strain levels, leading to the significantly leveraged strain-hardening curve.

4. Discussion

4.1. *Effect of Cu and Ni alloying on austenite reversion*

Cu and Ni are widely recognized as austenite stabilizing elements, which not only stabilize the austenite, but also increase the austenite fraction. However, most studies on the impact of Cu and Ni have focused on their effect on the mechanical stability of austenite. Choi et al. [47] alloyed Cu in a Fe-0.4C–15Mn (wt.%) austenitic high manganese steel with (0-1-2 wt.%) addition. They determined that the stacking fault energy of austenite increased by 1.52 mJ/m^2 with a 1 wt.% increase in Cu. Further, Ni effectively improved the mechanical stability of austenitic stainless steels.

In the present study, the effect of alloying 1.5 wt.% Cu and 1.5 wt.% Ni on the volume fraction of RA in the SA- and SAT-treated MMnS was obtained via SY-XRD measurements, as shown in Fig. 9. The error bar was obtained from Rietveld refinement calculation. Alloying Cu and Ni led to a more significant austenite reversion than that observed owing to the 0Cu0Ni-alloy. The 1.5Cu1.5Ni-alloy exhibited doubled austenite fraction (38.5 vol.%) than the 0Cu0Ni-alloy (19 vol.%) after the SAT process. On the one hand, the alloying of Cu and Ni lowered the A_{c1} temperature, so that the austenite fraction is increased in the 1.5Cu1.5Ni-alloy. On the other hand, the 1.5Cu1.5Ni-alloy showed a significant increase in austenite

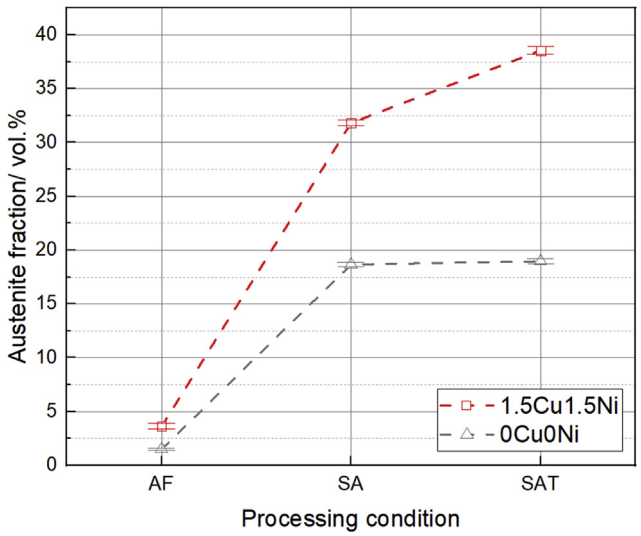

Fig. 9 – Effect of Cu–Ni alloying on the austenite fraction under different processing conditions.

fraction during the tempering step, while the RA fraction of the 0Cu0Ni-alloy exhibited a negligible increase. This could be attributed to the drag effect of Cu and Ni solute atoms on the austenite–ferrite phase boundaries [26,48]. According to the phase maps in Fig. 4, an increase in the austenite phase fraction is achieved by the coarsening of austenite laths. Cu and Ni atoms retarded the mobility of the austenite–ferrite laths interfaces, such that the austenite reversion did not reach the equilibrium in the SA step, and thus, continued in the tempering step. During the tempering step, Cu-rich precipitates precipitated from the ferrite phase, which lead to lower Cu concentration in the ferrite matrix of the 1.5Cu1.5Ni-SAT specimen (shown in Fig. 5c and d). Despite the composition between precipitation and partition, the alloying of Cu and Ni led to a significant increase in the austenite fraction during the tempering step. On the contrary, the austenite reversion of the 0Cu0Ni-alloy reached equilibrium in the SA step, such that it remained constant during the tempering step.

Furthermore, the volume fraction and mechanical stability of austenite are crucial for the tensile strength and elongation of SAT-treated specimens. The RA mechanical stability coefficient k is applied to quantify the mechanical stability of RA in terms of its pertained amount after necking [4]:

$$f_\gamma = f_{\gamma 0} \exp(-k\varepsilon) \quad (4)$$

where $f_{\gamma 0}$, f_γ, and k represent the austenite fraction before deformation, austenite fraction after strained to ε, and mechanical stability coefficient of RA, respectively. Generally, a higher k value corresponds to the lower mechanical stability of RA. In this study, to calculate the mechanical stability of RA, the RA fraction at necking is measured via SY-XRD and applied as f_γ. The true strain of each specimen is considered as ε. The calculated mechanical stability coefficient k of each specimen is listed in Fig. 10. The 1.5Cu1.5Ni-alloy exhibited lower k values than reference 0Cu0Ni-alloy, under both SAT and SA conditions. The addition of Cu and Ni not only significantly increased the volume fraction of the SAT

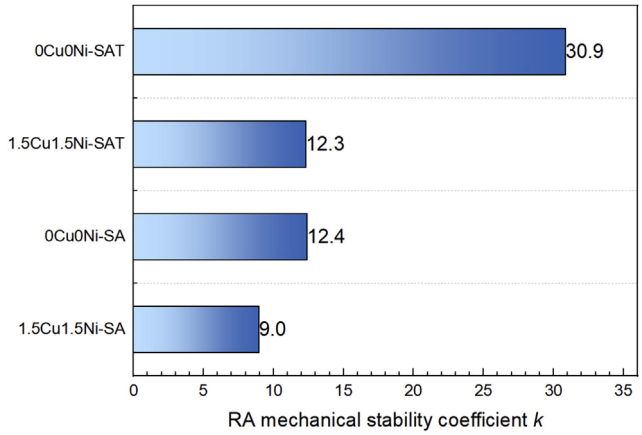

Fig. 10 – RA mechanical stability coefficient of the investigated specimens.

specimen (shown in Fig. 9), but also increased the mechanical stability of RA, which benefits the strain hardening during tensile deformation. Consequently, compared with the 0Cu0Ni-SAT specimen, the 1.5Cu1.5Ni-SAT specimen exhibited 226 MPa higher uniform tensile strength and 2.6% higher total elongation, which is due to the concurrent contribution of nano-precipitates and austenite reversion.

4.2. *Microstructure adjustment via the compact SAT treatment*

On the one hand, Cu and Ni are austenite stabilizers and can facilitate the austenite reversion. On the other hand, the Cu-rich precipitates can further strengthen the material. The α-γ partitioning of Cu and Ni should be considered when designing the intercritical annealing time and temperature since they are supposed to retain α to facilitate a high number density of nano-sized Cu-rich precipitates.

Recent studies have demonstrated that the Cu-rich precipitates can be achieved either during intercritical annealing (one-step) or in the subsequent tempering (multi-steps) [7,21,22]. For one-step annealing, when the intercritical annealing temperature is higher than the precipitation temperature, no Cu-rich precipitates can be formed in the matrix, and thus, the strength of the alloy cannot be increased. Austenite reversion is potentially suppressed when the intercritical annealing temperature is lower than the precipitation temperature, limiting the volume fraction of RA. For MMnS with more than 0.1 wt.% C, excellent tensile properties can be achieved through one-step intercritical annealing. Yan et al. [49] realized intercritical annealing on a Fe-0.12C-1.4Si-6.2Mn-0.93Ni-1.4Cu (in wt.%) MMnS at 620 °C for 1 h, achieving a UTS of 1200 MPa with 35% TE. However, such a high strength cannot be obtained via one-step annealing for MMnS with a carbon content lower than 0.05 wt.%, which resulted in an intercritical temperature higher than the precipitation temperature of Cu-rich precipitates. Therefore, two-step annealing is considered over one-step annealing in this study. In the intercritical annealing step, a sufficient amount of austenite is supposed to be reverted without the enrichment of Cu and Ni, such that it should be at a high temperature with a short holding time. Zou et al. [7] performed intercritical annealing on a Fe-0.05C-4.9Mn-0.6Si-0.04Al-1.55Ni-1.22Cu-0.05Nb-0.02Ti-0.002B MMnS at 600 °C for 1 h and achieved a YS of 1005 MPa with a UTS of 1070 MPa; the strain hardening ability is fairly limited.

To simultaneously achieve a high yield strength and high strain hardening rate, Kong et al. [22] designed a sophisticated processing route for Fe–8Mn–1Ni–2Cu–3Cr-1.1Si-0.8Mo-0.5Al-0.3Ti-0.11C-0.02B MMnS. First, the cold-rolled alloy was intercritical annealed at 700 °C for 10 min followed by water quenching, then intercritically annealed at 640 °C for 10 min followed by water quenching, and finally tempered at 500 °C for 2 h followed by water quenching. Although the alloy eventually exhibited a yield strength of 1130 MPa, UTS of 1370 MPa, and TE of 30%, the applied heat treatment route was complex.

In this study, with the applied compact SAT treatment, the alloying of Cu and Ni significantly increased the austenite fraction (from 19 vol.% to 38.5 vol.%). Meanwhile, the annealing is short (2 min) to prevent Cu and Ni from partitioning into austenite, since they are supposed to stay in ferrite phase and then promote the nano-precipitation in the subsequent tempering stage. Benefiting from the above-mentioned short annealing time, high number density (1.15×10^{23} m^{-3}) of nano-precipitates with Cu concentration of 20–50 at.% in the precipitation core and enriched with Cu, Ni, Al and Mn was observed by 3D-APT in the interior of ferrite phase, which significantly contributed to the rise of yield strength by precipitation strengthening. The incomplete partitioning of Cu, Ni, Al and Mn results in an adequate supersaturation in ferrite to trigger the nano-precipitation and continuation of austenite reversion transformation during tempering.

5. Summary and conclusions

The proposed "short annealing and tempering (SAT)" treatment is a compact process route for Cu and Ni containing medium-Mn steel (MMnS) to achieve excellent mechanical properties through the variation of a microstructure that comprises an adequate austenite fraction and Cu-rich precipitates. The low annealing time allowed for an incomplete partitioning of Cu and Ni from ferrite, which promoted the nano-precipitates during the subsequent tempering step. The notable conclusions are as follows:

(1) The proposed two-step heat treatment effectively helped achieve a considerable fraction of austenite in the very-low-C MMnS. The austenite fraction of 1.5Cu1.5Ni-alloy increased to 31.8 vol.% after short time annealing, which increased to 38.5 vol.% during the subsequent tempering. The alloying of 1.5 wt.% Cu and 1.5 wt.% Ni enhanced the austenite reversion during both SAT steps, by double that achieved with the reference alloy.
(2) The compact route resulted in an adequate supersaturation of Cu and Ni in ferrite to trigger the nano-precipitation during tempering. High number density (1.15×10^{23} m^{-3}) of nano-precipitates with Cu concentration of 20–50 at.% in the precipitation core and

enriched with Cu, Ni, Al and Mn were observed in the interior of the ferrite matrix, which contributed to the significantly increased yield strength by precipitation strengthening.

(3) The considerable amount of reverted austenite along with the formed nano-precipitates induced by Cu and Ni addition positively affected not only the strain hardening behavior, but also the whole tensile property profile of the investigated very-low-C MMnS. The increase in yield strength is primarily attributed to the formed nano-precipitates, while the enhanced ultimate tensile strength and the total elongation are primarily enhanced through activation of the transformation-induced plasticity (TRIP) effect controlled by the stability of the adjusted austenite.

Declaration of Competing Interest

The authors declare that they have no known competing financial interests or personal relationships that could have appeared to influence the work reported in this paper.

Acknowledgment

Zigan Xu is grateful for the financial support from the China Scholarship Council (CSC). Xiao Shen, Wenwen Song, and Wolfgang Bleck are thankful to the German Research Foundation (DFG) for their support within the project BL 402/49–1. We acknowledge DESY (Hamburg, Germany), a member of the Helmholtz Association HGF, for the provision of experimental facilities. Parts of this research were conducted at beamline P02.1 of PETRA III (proposal No. I-20191416). Finally, we would like to thank Martin Etter and Alexander Schökel for their support at the Beamline for SY-XRD measurement.

REFERENCES

[1] Ma Y. Medium-manganese steels processed by austenite-reverted-transformation annealing for automotive applications. Mater Sci Technol 2017;33:1713–27.
[2] Alexander Gramlich, Robin Emmrich, Wolfgang Bleck, Austenite reversion tempering-annealing of 4 wt.% manganese steels for automotive forging application, Metals 9 (5) 575.
[3] Su Guanqiao, Gao Xiuhua, Du Linxiu, Zhang Dazheng, Hu Jun, Liu Zhenguang. Influence of Mn on the corrosion behaviour of medium manganese steels in a simulated seawater environment. Int J Electrochem Sci 2016;11:9447–61.
[4] Lee Y-K, Han J. Current opinion in medium manganese steel. Mater Sci Technol 2015;31:843–56.
[5] Allam T, Bleck W, Klinkenberg C, Kintscher B, Krupp U. The continuous casting behavior of medium manganese steels. J Mater Res Technol 2021;15:292–305.
[6] Hu J, Zhang J, Sun G, Du L, Liu Y, Dong Y. High strength and ductility combination in nano-. Ultrafine-grained Medium-Mn Steel Tuning Stability Reverted Austenite Involving Intercritical Annealing 2019;54:6565–78.
[7] Zou Y, Xu YB, Han DT, Hu ZP, Misra RDK, Cao LF, et al. Combined contribution of Cu-rich precipitates and retained austenite on mechanical properties of a novel low-carbon medium-Mn steel plate. J Mater Sci 2019;54:3438–54.
[8] Kong H, Liu C. A review on nano-scale precipitation in steels. Technologies 2018;6:36.
[9] Hu J, Du L, Dong Y, Meng Q, Misra R. Effect of Ti variation on microstructure evolution and mechanical properties of low carbon medium Mn heavy plate steel. Mater Char 2019;152:21–35.
[10] Jiang S, Wang H, Wu Y, Liu X, Chen H, Yao M, et al. Ultrastrong steel via minimal lattice misfit and high-density nanoprecipitation. Nature 2017;544:460–4.
[11] Seol J-B, Na S-H, Gault B, Kim J-E, Han J-C, Park C-G, et al. Core-shell nano-particle arrays double the strength of steel. Sci Rep 2017;7:42547.
[12] Bhagat AN, Pabi SK, Ranganathan S, Mohanty ON. Aging behaviour in copper bearing high strength low alloy steels. ISIJ Int 2004;44:115–22.
[13] Jiao ZB, Luan JH, Miller MK, Chung YW, Liu CT. Co-precipitation of nanoscale particles in steels with ultra-high strength for a new era. Mater Today 2017;20:142–54.
[14] Jiao ZB, Luan JH, Miller MK, Liu CT. Precipitation mechanism and mechanical properties of an ultra-high strength steel hardened by nanoscale NiAl and Cu particles. Acta Mater 2015;97:58–67.
[15] Gyakwaa F, Alatarvas T, Shu Q. Characterization of synthetic non-metallic inclusions consisting of TiN, Ti_2O_3, and oxides of Al_2O_3 and $MgO{\cdot}Al_2O_3$ spinel using Raman spectroscopy. Metals 2021;11:1549.
[16] Liu CT, Jiao ZB, Luan JH. Copper-rich nanoclusters: ferritic steels strengthened, encyclopedia of iron, steel and their alloys. CRC Press, Taylor & Francis Group; 2015pp875–86.
[17] Zhang Z, Liu CT, Miller MK, Wang X-L, Wen Y, Fujita T, et al. A nanoscale co-precipitation approach for property enhancement of Fe-base alloys. Sci Rep 2013;3:1327.
[18] Z. B. Jiao, J. H. Luan, M. K. Miller, C. Y. Yu, C. T. Liu, Group precipitation and age hardening of nanostructured Fe-based alloys with ultra-high strengths, Sci Rep 6 1–13.
[19] Jiao ZB, Luan JH, Zhang ZW, Miller MK, Ma WB, Liu CT. Synergistic effects of Cu and Ni on nanoscale precipitation and mechanical properties of high-strength steels. Acta Mater 2013;61:5996–6005.
[20] Li Y, Li W, Liu W, Wang X, Hua X, Liu H, et al. The austenite reversion and co-precipitation behavior of an ultra-low carbon medium manganese quenching-partitioning-tempering steel. Acta Mater 2018;146:126–41.
[21] Cheng P, Hu B, Liu SL, Guo H, Enomoto M, Shang CJ. Influence of retained austenite and Cu precipitates on the mechanical properties of a cold-rolled and intercritically annealed medium Mn steel. Mater Sci Eng, A 2019;746:41–9.
[22] Kong HJ, Yang T, Chen R, Yue SQ, Zhang TL, Cao BX, et al. Breaking the strength-ductility paradox in advanced nanostructured Fe-based alloys through combined Cu and Mn additions. Scripta Mater 2020;186:213–8.
[23] Allam T, Guo X, Sevsek S, Chwałek M, Bleck W. Development of a Cr-Ni-V-N medium manganese steel with balanced mechanical and corrosion properties. Metals 2019;9:705.
[24] Dieudonné T, Marchetti L, Wery M, Miserque F, Tabarant M, Chêne J. Role of copper and aluminum on the corrosion behavior of austenitic Fe–Mn–C TWIP steels in aqueous solutions and the related hydrogen absorption. Corrosion Sci 2014;83:234–44.
[25] Allam T, Bleck W. Development of a new concept for hot-rolled weathering–DP steel: thermo-mechanical simulation, microstructure adjustment, and mechanical properties. Steel Res Int 2016;87:68–78.

[26] Sun M, Zhang W, Liu Z, Wang G. Influence of Cu on microstructure and mechanical properties for an extremely low carbon steel during isothermal process. steel research int 2017;88:1600344.
[27] Ren L, Nan L, Yang K. Study of copper precipitation behavior in a Cu-bearing austenitic antibacterial stainless steel. Mater Des 2011;32:2374–9.
[28] Xu Z, Shen X, Allam T, Song W, Bleck W. Austenite transformation and deformation behavior of a cold-rolled medium-Mn steel under different annealing temperatures. Mater Sci Eng, A 2021:142115.
[29] Xu Z, Li J, Shen X, Allam T, Richter S, Song W, et al. Tailoring the austenite fraction of a Cu and Ni containing medium-Mn steel via warm rolling. Metals 2021;11:1888.
[30] Escobar JD, Oliveira JP, Salvador CAF. Meta-equilibrium transition microstructure for maximum austenite stability and minimum hardness in a Ti-stabilized supermartensitic stainless steel. Mater Des 2018;156:609–21.
[31] Hammersley AP. FIT2D a multi-purpose data reduction, analysis and visualization program. J Appl Crystallogr 2016;49:646–52.
[32] Gražulis S, Chateigner D, Downs RT, Yokochi AFT, Quirós M, Lutterotti L, et al. Crystallography Open Database - an open-access collection of crystal structures. Journal of applied crystallography3 2009;42:726–9.
[33] Lutterotti L. Maud: a Rietveld analysis program designed for the internet and experiment integration. Acta Crystallogr A 2000;56:s54.
[34] Goodman SR, Brenner SS, Low JR. An FIM-atom probe study of the precipitation of copper from lron-1.4 at. pct copper. Part I: field-ion microscopy. Metall Trans A 1973;4:2363–9.
[35] Goodman SR, Brenner SS, Low JR. FIM [field-ion microscope] atom probe study of the precipitation of copper from iron-1.4 atomic pct. copper. II. Atom probe analyses. Metall Trans A 1973;4:2371–8.
[36] Buswell JT, English CA, Phythian MG, Smith WJ, Worrall GM. Proceedings of the 14th international symposium on effects of radiation on materials. ASTM Special Technical; 1988. p. 127–53.
[37] Lee TH, Kim YO, Kim SJ. Crystallographic model for bcc-to-9R martensitic transformation of Cu precipitates in ferritic steel. Phil Mag 2007;87:209–24.
[38] Heo Y-U, Kim Y-K, Kim J-S, Kim J-K. Phase transformation of Cu precipitates from bcc to fcc in Fe–3Si–2Cu alloy. Acta Mater 2013;61:519–28.
[39] Miller MK, Pareige P, Burke MG. Understanding pressure vessel steels: an atom probe perspective. Mater Char 2000;44:235.
[40] Pareige P, Russell KF, Miller MK. APFIM studies of the phase transformations in thermally aged ferritic FeCuNi alloys: comparison with aging under neutron irradiation. Appl Surf Sci 1996;94– 95:362.
[41] Pareige P, Miller MK. Characterization of neutron-induced copper-enriched clusters in pressure vessel steel weld: an APFIM study. Appl Surf Sci 1996;94–95:370.
[42] Isheim D, Fine ME, Seidman DN. Acquisition of a local-electrode atom-probe (LEAP) microscope (an atom-probe tomograph) for three-dimensional nanoscale characterization of materials. Microsc Microanal 2007;13:1624.
[43] Isheim D, Gagliano MS, Fine ME, Seidman DN. Interfacial segregation at Cu-rich precipitates in a high-strength low-carbon steel studied on a sub-nanometer scale. Acta Mater 2006;54:841.
[44] Nagano T, Enomoto M. Simulation of the growth of copper critical nucleus in dilute bcc Fe–Cu alloys. Scripta Mater 2006;55:223.
[45] Fine ME, Isheim D. Origin of copper precipitation strengthening in steel revisited. Scripta Mater 2005;53:115–8.
[46] Nakashima k, Futamura Y, Tsuchiyama T, Takaki S. Interactions between dislocation and Cu particle in Fe-Cu alloys. ISIJ int 2002;42:1541–5.
[47] Choi JH, Jo MC, Lee H, Zargaran A, Song T, Sohn SS, et al. Cu addition effects on TRIP to TWIP transition and tensile property improvement of ultra-high-strength austenitic high-Mn steels. Acta Mater 2019;166:246–60.
[48] Arribas M, Gutiérrez T, Del Molino E, Arlazarov A, de Diego-Calderón I, Martin D, et al. Austenite reverse transformation in a Q&P route of Mn and Ni added steels. Metals 2020;10:862.
[49] Yan S, Liang T, Chen J, Li T, Liu X. A novel Cu-Ni added medium Mn steel: precipitation of Cu-rich particles and austenite reversed transformation occurring simultaneously during ART annealing. Mater Sci Eng, A 2019;11:73–81.